

Parameter estimation of hairy Kerr black holes from its shadow and constraints from M87*

Misba Afrin^{a,*}, Rahul Kumar^{a,†} and Sushant G. Ghosh^{a,b,‡}

^a Centre for Theoretical Physics, Jamia Millia Islamia, New Delhi 110025, India and

^b Astrophysics and Cosmology Research Unit, School of Mathematics, Statistics and Computer Science, University of KwaZulu-Natal, Private Bag 54001, Durban 4000, South Africa

The recently obtained hairy Kerr black holes, due to additional sources or surrounding fluid, like dark matter, conserving energy-momentum tensor, are with a deviation α , and primary hair l_0 apart from rotation parameter a and mass M . The Event Horizon Telescope (EHT) has released the first image of supermassive black hole M87*, revealing that the observed image is consistent with the shadow of a Kerr black hole and has opened up a new window to probe the strong gravity regime. In the wake of the EHT observations, the recent interest in black hole shadow suggests comparing the black holes in general relativity (GR) and modified theories of gravity to assess these models' differences. Motivated by this, we consider the rotating hairy Kerr black holes, which encompasses, in particular cases, Kerr ($\alpha = 0$) black holes. Interestingly, for a set of parameters (M , a , and α), there exists an extremal value of the hair parameter l_E , which corresponds to an extremal black hole with degenerate horizons. In contrast, for $l_0 > l_E$, it describes a nonextremal black hole with Cauchy and event horizons and a naked singularity for $l_0 < l_E$. We investigate ergosphere and shadow of hairy Kerr black holes to infer that their size and shape are affected due to the l_0 and have a richer chaotic structure. In particular, the hairy Kerr black holes possess smaller size but more distorted shadows when compared with Kerr black holes. We also estimate the parameters l_0 and a associated with hairy Kerr black holes using the shadow observables. We show that the inferred circularity deviation $\Delta C \leq 0.1$ for the M87* black hole puts a constraint on hairy Kerr black hole parameter a , whereas angular shadow diameter $\theta_d = 42 \pm 3\mu as$, within 1σ region, for a given choice of α , also places bounds on these parameters.

I. INTRODUCTION

Recently, the international Event Horizon Telescope (EHT) collaboration has unveiled the first shadow image of a supermassive black hole M87* with angular size gravitational radius $3.8 \pm 0.4 \mu as$ – an asymmetric bright emission ring with a diameter of $42 \pm 3 \mu as$, exhibiting a deviation from circularity $\Delta C \leq 0.1$ and an axis ratio $\lesssim 4/3$, and it is consistent with the shadow of a Kerr black hole of general relativity. The black hole shadows have become a physical reality with the detection of the M87* black hole's horizon-scale image [1–3]. The bright, sharp photon ring, a projection along the photons' null geodesics orbiting around the black hole, encompasses the shadow and explicitly depends on the black hole parameters [4]. It has been found that the quantitative features are not sufficient to distinguish between black holes using different theories of gravity. Thus, using the M87* black hole shadow, one can investigate the viability of black holes in modified theories of gravity (MoG) in explaining the observational data and constraints on the black hole parameters and the EHT observations thus became an important tool to test strong gravitational fields.

The shadow of rotating black holes attracted a lot of attention in the last decades, led by the seminal work by Synge [5] and Lunin [6], who gave the formula to calculate the angular radius of the photon capture region around the Schwarzschild black hole. Later, Bardeen [7] analysed the shadow of the Kerr black hole and showed that the spin would cause distortion in the shape of shadows. Applications of shadow in unravelling the useful information regarding the near horizon features of gravity have aroused a flurry of activities in the analytical investigations, and numerical simulation of shadows for black holes in GR [8–17], some other configurations of black holes arising in modified theories of gravity (MoG) [18–25] and in higher dimensions [26–28]. One of the motivations of several works on black hole shadow is that the trajectories of light near black holes are related to the background geometry's essential features and properties. Moreover, by observing the size and deformation of its shadow, the spin, mass parameter and possibly other global charges or *hair*-parameters of the black holes can be calculated [17, 29–32]. Moreover, it is also useful in testing theories of gravity [33].

*Electronic address: me.misba@gmail.com

†Electronic address: rahul.phy3@gmail.com

‡Electronic address: sghosh2@jmi.ac.in, sghosh@gmail.com

Observations of the shadow of supermassive black holes M87* allow us to study the properties of black holes and the nature of strong-field gravity. In principle, one can use black hole shadow observations to place constraints on the hairy Kerr black hole, which can also be a solution to modified gravity theories that do not admit the Kerr solution. We here investigate, whether black hole shadow observations can constrain hairy Kerr black holes [34], which has additional deviation parameters α and primary hair l_0 , from the Kerr black hole. Furthermore, we investigate the horizons, ergoregions and shadow cast by the hairy Kerr black holes [34]. We obtain the null geodesics equations of motions in the first-order differential form using the Hamilton-Jacobi approach, and the analytical expressions for the photon region are also determined. An investigation of the deviation parameters' effects shows that the hairy Kerr black holes cast smaller and more distorted shadows than those for the Kerr black holes. In turn, we use shadow observables to characterize the shadows' size and shape and estimate the black hole parameters a and l_0 . The M87* black hole shadow results, inferred from the recent Event Horizon Telescope (EHT) collaborations observations, are further used to constrain the parameters a and l_0 .

The hairy Kerr black hole that we are interested in, is obtained using the gravitational decoupling approach [34]. It has a source satisfying the strong energy condition (SEC) and gives an extended Kerr metric which was termed as Kerr black holes with primary hair by Contreras *et. al.* [34]. Hairy black holes are termed as stationary black hole solution with new global charges, which are not associated with Gauss law [35], e.g., black holes with scalar hair [36, 37], or proca hair [38]. See Ref. [35] for a recent review on black holes with hair due to global charge.

This paper is organized as follows. In the Sec. II, we consider hairy black holes, discuss the effect of l_0 , for given choice of α , on horizon structure and ergoregions. Sec. III is devoted to the brief review of the null geodesic equations in the hairy Kerr black hole spacetimes. The impact of the hair parameter l_0 on the black hole shadow is the subject of Sec. IV. We present the observables for shadow characterization and use them to estimate the parameters associated with hairy Kerr black holes in Sec. V, and assuming M87* as hairy Kerr black holes, we calculate the circularity deviation and angular diameter observable over the entire parameter space for $\theta_0 = \pi/2$ in Sec. VI. Finally, we summarize our main findings in Sec. VII. We use geometrized units $G = 1, c = 1$, unless units are specifically defined.

II. HAIRY KERR BLACK HOLES

The Gravitational Decoupling (GD) approach is precisely designed to find deformation of the known solution of GR due to the additional surrounding sources like dark matter or dark energy [34] (see also [39, 40]). The GD approach leads to deformed or hairy Schwarzschild black holes [34] given by

$$ds^2 = - \left[1 - \frac{2M}{r} + \alpha e^{-r/(M-\frac{l_0}{2})} \right] dt^2 + \frac{1}{\left[1 - \frac{2M}{r} + \alpha e^{-r/(M-\frac{l_0}{2})} \right]} dr^2 + r^2(d\theta^2 + \sin^2\theta d\phi^2). \quad (1)$$

Here, M is the black hole mass, α is the deviation parameter and $l_0 \leq 2M$, which ensures asymptotic flatness, corresponds to primary hair. The surrounding matter that leads to deformation of the Schwarzschild black holes (1) is described by the conserved stress-energy tensor $S_{\mu\nu}$ that satisfies the strong energy condition (SEC). The hairy black hole (1) encompasses the Schwarzschild black hole in the absence of the surrounding matter ($\alpha = 0$). The rotating black hole solutions in modified gravity theories are essential as they offer an arena to test these theories through astrophysical observation. There is hardly any test for non-rotating solutions since the black hole spin is crucial in any astrophysical process.

Hence, we consider the rotating counterpart of the spherically symmetric solution. The stationary and axisymmetric counterpart of the spherically symmetric solution (1) described by parameters M, a, l_0 and α , in the Boyer-Lindquist coordinates reads [34]

$$ds^2 = - \left[\frac{\Delta - a^2 \sin^2 \theta}{\Sigma} \right] dt^2 - 2a \sin^2 \theta \left[1 - \frac{\Delta - a^2 \sin^2 \theta}{\Sigma} \right] dt d\phi \\ + \sin^2 \theta \left[\Sigma + a^2 \sin^2 \theta \left(2 - \frac{\Delta - a^2 \sin^2 \theta}{\Sigma} \right) \right] d\phi^2 + \frac{\Sigma}{\Delta} dr^2 + \Sigma d\theta^2, \quad (2)$$

with $\Delta = r^2 + a^2 - 2Mr + \alpha r^2 e^{-r/(M-\frac{l_0}{2})}$ and $\Sigma = r^2 + a^2 \cos^2 \theta$, where a denotes the angular momentum. The α is a generic parameter that measures potential deviation of metric 2 from the standard Kerr black holes and is related to l_0 via $l_0 = \alpha l$. The black hole 2 is termed as hairy Kerr black holes [34] which encompasses the Kerr black hole in the absence of surrounding matter ($\alpha = 0$). The solution 2 results from the surrounding matter described by stress tensor $S_{\mu\nu}$ satisfying the strong energy conditions. Thus metric (2) can be seen as a prototype non-Kerr black hole and with an additional deviation parameter α and primary hair l_0 [34]. When written in Boyer-Lindquist coordinate,

it is same as Kerr black hole with M replaced by $m(r) = M - \frac{\alpha}{2} r e^{-r/(M-\frac{l_0}{2})}$. In what follows, we shall investigate how primary hair l_0 affects the Kerr horizons and shadow.

The metric 2 is singular at spacetime points where $\Sigma \neq 0$ and $g^{\alpha\beta} \partial_\alpha r \partial_\beta r = g^{rr} = \Delta = 0$, which corresponds to the event horizon. Thus zeros of

$$r^2 + a^2 - 2Mr + \alpha r^2 e^{-r/(M-\frac{l_0}{2})} = 0, \quad (3)$$

give the black hole horizons. Equation (3), when $\alpha = 0$ (Kerr black hole), admits solutions

$$r_{\pm} = M \pm \sqrt{M^2 - a^2}. \quad (4)$$

Here, r_+ denotes outer (event) horizon and r_- the inner (Cauchy) horizon. It is clear that the metric (2) describes non-extremal black hole for $r_+ > r_-$ and when $r_+ = r_-$, one obtains an extremal black hole. To ensure the event horizon's existence, we require $M \geq a$. It defines a region, parameter space, where metric represents a black hole and not a naked singularity. The case $M < a$, contains a naked singularity.

Numerical analysis of Eq. (3) reveals that depending on the values of M , a , α and l_0 there can exist a maximum of two distinct real positive roots, or equal roots, or no-real positive roots. They respectively correspond to the non-extremal black holes with Cauchy and event horizons, extremal black holes, and no-black holes scenarios. The degenerate condition of the horizons gives a bound on the black hole parameters l_0 and a and the (l_0-a) parameter space is shown in Fig. 1.

From the horizon structure of the hairy Kerr black holes depicted in Fig. 2, it turns out that, for given values of α and l_0 , there exists critical extremal value of a , a_E and likewise there exists critical extremal value of l_0 , l_E for given value of α and a , where $\Delta = 0$ has a double root. The hairy Kerr black hole exists when $a < a_E$ while for $a > a_E$ there is a naked singularity and the a_E depends on l_0 , e.g., for $l_0 = 0.2M, 0.5M$ respectively, $a_E = 0.8350M, 0.8638M$. Also $l_0 > l_E$ corresponds to hairy Kerr black holes with Cauchy and event horizons whereas $l_0 < l_E$ implies existence of a naked singularity. It may be noted that, for $a = 0.85M, 0.90M$, $l_E = 0.3562M, 0.7778M$ respectively. Indeed a_E increases with the increase in l_0 likewise l_E increases with increase in a . For fixed values of M , a and l_0 , the hairy Kerr black holes have decreasing event horizon radius and increasing Cauchy horizon radius with the increase in deviation parameter α from the Kerr limit, $\alpha = 0$ (cf. Fig. 2). Thus the hairy Kerr black holes have smaller event horizon radii than the Kerr black hole. At the extremal value $\alpha = \alpha_E$, the two horizons coincide and the radius of this extremal event horizon (r_E) increases with the increase in rotational parameter a while the value of α_E decreases, for e.g., $\alpha_E = 1.8283$, $r_E = 0.6009M$ for $a = 0.7M$ and $\alpha_E = 1.1652$, $r_E = 0.7615M$ for $a = 0.8M$ (cf. Fig. 2).

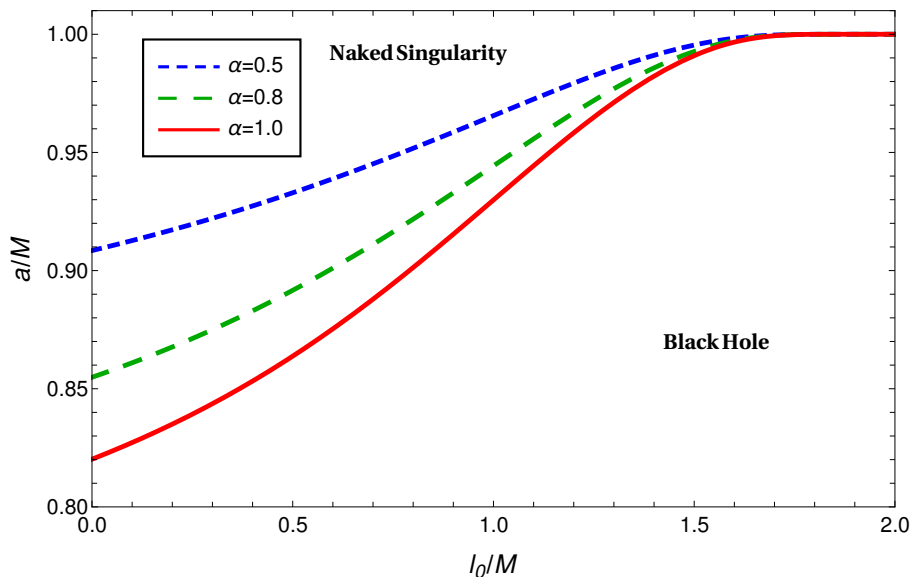


Figure 1: $l_0 - a$ parameter space of the hairy Kerr black hole. The lines separate black holes from naked singularity ($\Delta = 0$ has no real root).

On the other hand, at the static limit surface (SLS), the asymptotic time-translational Killing vector $\chi^i = (\frac{\partial}{\partial t})^i$, becomes null, i.e.,

$$\chi^i \chi_i = g_{tt} = r^2 + a^2 \cos^2 \theta - 2Mr + \alpha r^2 e^{-r/(M-\frac{l_0}{2})} = 0. \quad (5)$$

Thus, the location of SLS are the real positive roots (r_{SLS}^{\pm}) of Eq. (5) which admits two possible. The larger of the two roots corresponds to the outer surface of the SLS, denoted by r_{SLS}^+ . The analysis of the zeros of Eq. (5), for a given values of a , l_0 and θ , disseminate a critical parameter α_{SLS}^E such that Eq. (5) has no root if $\alpha > \alpha_{SLS}^E$, a double root at $\alpha = \alpha_{SLS}^E$, and two simple roots if $\alpha < \alpha_{SLS}^E$.

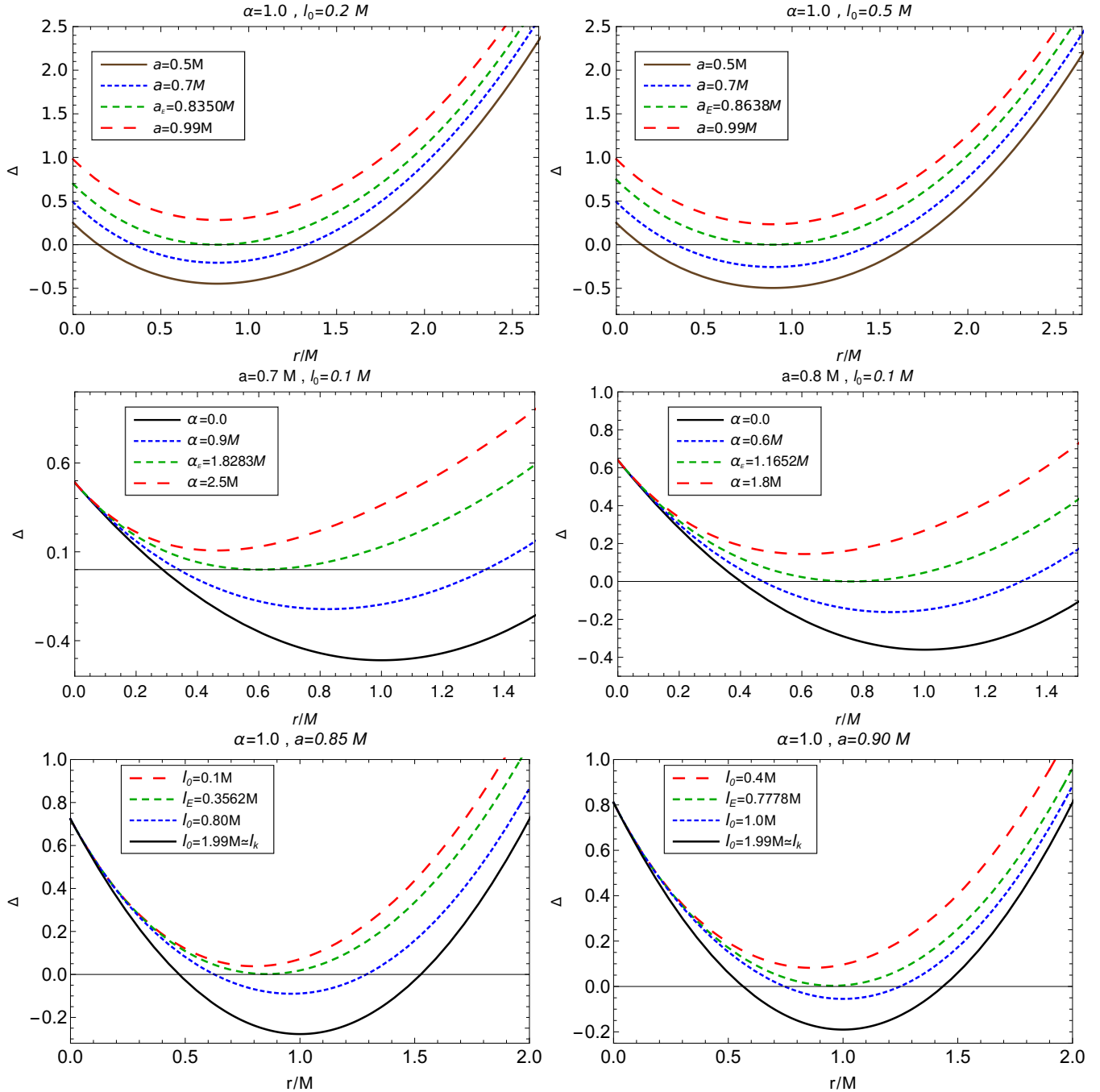


Figure 2: Horizons of the hairy Kerr black holes are shown with varying a [top], α [middle] and l_0 [bottom] and compared with the Kerr black holes ($\alpha = 0$ or $l = l_k$).

The ergoregion bounded between $r_+ < r < r_{SLS}^+$, where the timelike killing vector χ^i becomes spacelike, and an observer necessarily follows the worldline of χ^i , has been shown in Fig. 3 for the hairy Kerr black hole (2). The parameter l_0 has a diminishing effect on the ergosphere's size, as the ergoregion gets smaller with the increase in l_0 for fixed values of the parameters α and a . Thus, the hairy Kerr black holes have smaller ergoregions than the Kerr

black hole ($l = l_k$). Moreover, in the non-Kerr limit ($l_0 \neq l_k$), the increase in the α increases the size of the ergoregion at fixed values of l_0 and a . It is also worthwhile noting that the decrease in the parameter l_0 leads to disconnected event horizons for fast rotating hairy Kerr black holes (cf. Fig. 3). The ergoregion acquired its name owing to the theoretical possibility of extracting energy and mass from this region via the Penrose process [41].

The frame dragging effect of the hairy Kerr black hole becomes evident from the off diagonal elements of metric (2) viz., $g_{t\phi}$. Due to this effect, a stationary observer outside the event horizon, moving with zero angular momentum with respect to an observer at spatial infinity can rotate with the black hole with an angular momentum given by [42]

$$\tilde{\omega} = \frac{d\phi}{dt} = -\frac{g_{t\phi}}{g_{\phi\phi}} = \frac{2ar(M - \alpha\frac{r}{2}e^{-r/(M-\frac{l_0}{2})})}{(r^2 + a^2)^2 - a^2\Delta\sin^2\theta}, \quad (6)$$

which monotonically increases as the observer approaches the black hole and ultimately at the event horizon, where the observer begins co-rotating with the black hole, takes the maximum value:

$$\Omega = \tilde{\omega}|_{r=r_+} = \frac{2ar_+(M - \alpha\frac{r_+}{2}e^{-r_+/(M-\frac{l_0}{2})})}{(r_+^2 + a^2)^2}. \quad (7)$$

Here ω is the black hole angular velocity, which in the limit $\alpha = 0$ reads

$$\Omega_{Kerr} = \frac{2Mar_+}{(r_+^2 + a^2)^2} \quad (8)$$

and corresponds to the angular velocity of Kerr black hole [43]. It is clear that each point of the horizon has the same angular velocity (as measured at the infinity) and in this sense the surface of the black hole is rotating as a rigid body [43]

III. GEODESICS AROUND ROTATING BLACK HOLES

The geodesic motion of photons around the black hole is necessary to study the shadow formation, and for this purpose, we consider a motion of test particle in stationary and axially symmetric spacetime. Since metric (2) doesn't depend on t and ϕ , hence these are cyclic coordinates and corresponding killing vectors are given by $\chi_{(t)}^\mu = \delta_t^\mu$ and $\chi_{(\phi)}^\mu = \delta_\phi^\mu$, whose existence further implies that the corresponding momenta p_t and p_ϕ are constants of motion. The motion of the test particle, neglecting the back reaction, is determined by the rest mass m_0 , total energy E , angular momentum L_z and Carter constant \mathcal{Q} which associated with the second-rank irreducible tensor field of hidden symmetry [44]. We use the Hamilton-Jacobi equation following the integral approach pioneered by Carter [44] to obtain the geodesic equations in the first-order differential form, which for the metric (2) read [45]

$$\Sigma \frac{dt}{d\lambda} = \frac{r^2 + a^2}{\Delta} (E(r^2 + a^2) - aL_z) - a(aE\sin^2\theta - L_z), \quad (9)$$

$$\Sigma \frac{d\phi}{d\lambda} = \frac{a}{\Delta} (E(r^2 + a^2) - aL_z) - (aE - \frac{L_z}{\sin^2\theta}), \quad (10)$$

$$\Sigma \frac{dr}{d\lambda} = \pm \sqrt{\mathcal{R}(r)}, \quad (11)$$

$$\Sigma \frac{d\theta}{d\lambda} = \pm \sqrt{\Theta(\theta)}, \quad (12)$$

where λ is the affine parameter along the geodesics and the effective potentials $\mathcal{R}(r)$ and $\Theta(\theta)$ for radial and polar motion are given by

$$\mathcal{R}(r) = E^2 \left[\left((r^2 + a^2) - a\xi \right)^2 - \Delta \left(\eta + (a - \xi)^2 \right) \right], \quad (13)$$

$$\Theta(\theta) = E^2 \left[\eta - \left(\frac{\xi^2}{\sin^2\theta} - a^2 \right) \cos^2\theta \right]. \quad (14)$$

The constant \mathcal{K} is the separability constant related to the Carter constant \mathcal{Q} through $\mathcal{Q} = \mathcal{K} + (aE - L_z)^2$ [45]. We introduce dimensionless quantities called impact parameters [45]

$$\xi = \frac{L_z}{E}, \quad \eta = \frac{\mathcal{K}}{E^2}, \quad (15)$$

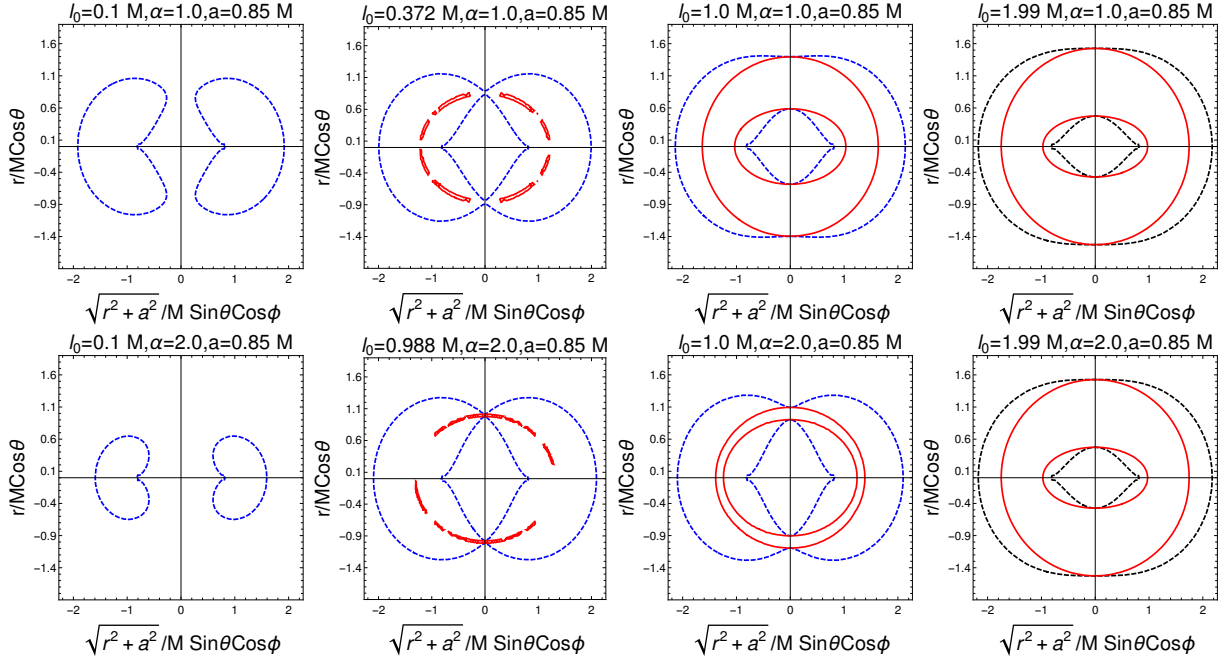


Figure 3: The cross-section of event horizon (outer red line), SLS (outer blue dotted line) and ergoregion of hairy Kerr black holes. The black dotted curves correspond to event horizon of Kerr black hole ($l_0 = l_k$)

which are constant along the geodesics. The allowed region for photon motion is $\mathcal{R} \geq 0$ and $\Theta(\theta) \geq 0$ and the sign of \dot{r} and $\dot{\theta}$ can be independently chosen to be either positive or negative. The change of sign occurs at turning points of motion, i.e. when $\mathcal{R} = 0$ or $\Theta = 0$ [45]. Depending on the critical parameters' values, the photon may either get captured, scatter to infinity, or form bound orbits. Here, we are interested in spherical lightlike geodesics on a sphere of constant coordinate radius r characterized by $\dot{r} = 0$ and $\ddot{r} = 0$ called the spherical photon orbits. Mathematically, this corresponds to the extremum of the radial potential at the unstable photon orbit radius $r = r_p$ such that [45, 46]

$$\mathcal{R} = \mathcal{R}' = 0 \text{ and } \mathcal{R}'' \leq 0. \quad (16)$$

Solving Eq. (16) results into the critical values of impact parameters (ξ_{crit}, η_{crit}) for the unstable orbits

$$\begin{aligned} \xi_{crit} &= \frac{(a^2 + r^2) \Delta'(r) - 4r\Delta(r)}{a\Delta'(r)}, \\ \eta_{crit} &= \frac{r^2 (8\Delta(r) (2a^2 + r\Delta'(r)) - r^2 \Delta'(r)^2 - 16\Delta(r)^2)}{a^2 \Delta'(r)^2}, \end{aligned} \quad (17)$$

where $'$ stands for the derivative concerning the radial coordinate, Eq. (17), in the limit $\alpha \rightarrow 0$, reduces to the critical impact parameter for the Kerr black holes [29]. The unstable photon orbits have been particularly studied with much interest for black holes and naked singularities [47–53] and in the case of the black hole, they define the boundary between the capture or no-capture of a cross-section of light rays. There can be two circular photon orbits in the equatorial plane of the black hole viz in axially symmetric spacetimes viz. those move in the same direction as the black hole's rotation and those moving the opposite it which are respectively called the prograde and retrograde photons. The prograde orbits being smaller in radius than the retrograde ones [54], which can be attributed to the Lens-Thirring effect [55], whereby, due to the dragging of the inertial frame by the black hole's rotation, to an observer at infinity, the prograde photons must have smaller orbits to account for the excess angular momentum. In contrast, the retrograde ones, having lost some angular momentum effectively, would have to rotate at larger radii [53]. The non-planar or 3-dimensional photon orbits only arise for $\eta_{crit} > 0$ whereas, for $\eta_{crit} = 0$, the photon orbits are planar and confined to the equatorial plane only. The radii of prograde (r_p^-) and retrograde (r_p^+) orbits at the equatorial

plane are obtained as roots of $\eta_{crit} = 0$. It turns out that these radii for the Kerr black holes are [53]

$$r_p^- \equiv 2M \left[1 + \cos \left(\frac{2}{3} \arccos \left(-\frac{|a|}{M} \right) \right) \right], \quad (18)$$

$$r_p^+ \equiv 2M \left[1 + \cos \left(\frac{2}{3} \arccos \left(\frac{|a|}{M} \right) \right) \right], \quad (19)$$

and they fall in the range $M \leq r_p^- \leq 3M$ and $3M \leq r_p^+ \leq 4M$ [17]. In the case of Schwarzschild black hole ($a = 0$) the two radii degenerate into a photon sphere of constant radius $r_p^- = r_p^+ = 3M$ [56]. While $r_p^+ > r_+$, all spherical photon orbits are confined to the region $r_p^- < r_p < r_p^+$. For the $\eta_{crit} > 0$ scenario, the non-planar ($\theta \neq \frac{\pi}{2}$ and $\dot{\theta} \neq 0$) geodesics have an additional latitudinal motion governed by the Carter constant which accounts for a hidden space-time symmetry. Furthermore, these orbits oscillate symmetrically about the equatorial plane while repeatedly crossing it.

IV. SHADOW OF HAIRY KERR BLACK HOLES

The black hole shadow is the optical appearance of the black hole caused by the strong gravitational lensing [57–63] of light near these compact objects and appears as a two-dimensional dark zone for an observer (for details see [64–67] and references therein). The shape and the size of the shadow depend on the parameters associated with the geometry of black hole spacetime. The shadow, in turn, has facilitated the estimation and measurement of various black hole parameters like its mass, spin angular momentum as well as other *hairs* [17]. Thus, it is a tool to test Einstein's GR in the strong-field regime [25, 68], and also the no hair theorem [69]. The photon region around the black hole's event horizon is formed from the combination of all unstable and spherical photon orbits, i.e. the separatrix between photon geodesics that escape to spatial infinity and those that fall into the event horizon.

We assume uniformly distributed light sources at infinity and the photons coming at all possible impact parameters and either getting scattered near the vicinity of the black hole (2) or captured by it. We also assume the observer at spatial infinity, at an inclination angle θ_0 with the rotation axis of the black hole. The celestial coordinates (X, Y) of the observer are the apparent angular distances of the image measured from the line of sight in directions perpendicular and parallel respectively, to the projected axis of rotation black hole onto the celestial sphere [29]. By making a stereographic projection of black hole shadow on the observer's celestial sky to the image plane, the shadow boundary can be described by the following coordinates

$$\begin{aligned} X &= \lim_{r_o \rightarrow \infty} \left(-r_o^2 \sin \theta_o \frac{d\phi}{dr} \right), \\ Y &= \lim_{r_o \rightarrow \infty} \left(r_o^2 \frac{d\theta}{dr} \right), \end{aligned} \quad (20)$$

where r_o is the distance between the observer and the black hole. For an asymptotic observer, Eq. (20) leads to

$$\begin{aligned} X &= -\xi_{crit} \csc \theta_o, \\ Y &= \pm \sqrt{\eta_{crit} + a^2 \cos^2 \theta_o - \xi_{crit}^2 \cot^2 \theta_o}. \end{aligned} \quad (21)$$

Further, if the observer in the equatorial plane ($\theta = \pi/2$), it simplifies to

$$\begin{aligned} X &= -\xi_{crit}, \\ Y &= \pm \sqrt{\eta_{crit}}. \end{aligned} \quad (22)$$

The contour of X and Y delineates the shadow for the hairy Kerr black holes. Eq. (22), on using metric (1), yields

$$\begin{aligned} X &= -\frac{[a^2 - 3r_p^2]m(r_p) + r_p[a^2 + r_p^2][1 + m'(r_p)]}{a[m(r_p) + r_p[-1 + m'(r_p)]]}, \\ Y &= \pm \frac{1}{a[m(r_p) + r_p[-1 + m'(r_p)]]} \left[r_p^{3/2} \left[-r_p^3(1 + m'(r_p)^2) \right. \right. \\ &\quad \left. \left. + m(r_p)[4a^2 + 6r_p^2 - 9r_p m(r_p)] - 2r_p[2a^2 + r_p^2 \right. \right. \\ &\quad \left. \left. - 3r_p m(r_p)]m'(r_p) \right]^{1/2} \right], \end{aligned} \quad (23)$$

where for brevity, we have used $m(r) = M - \frac{\alpha}{2} r e^{-r/(M - \frac{l_0}{2})}$. and whereas for the Kerr case, Eq. (23) simplifies to

$$\begin{aligned} X &= \frac{r_p^2(r_p - 3M) + a^2(M + r_p)}{a(r_p - M)}, \\ Y &= \pm \frac{r_p^{3/2}(4a^2M - r_p(r_p - 3M)^2)^{1/2}}{a(r_p - M)} \end{aligned} \quad (24)$$

which is exactly the same as obtained for the Kerr black hole [29], which for the nonrotating black hole (1) takes the form

$$X^2 + Y^2 = \frac{2r_p^4 + [m(r_p) + r_p m'(r_p)][-6r_p^2 m(r_p) + 2r_p^3 m'(r_p)]}{[m(r_p) + r_p[-1 + m'(r_p)]]^2}. \quad (25)$$

The Eq. (25) ensures that the shadow of a nonrotating black hole (1) is evidently a perfect circle and further Eq. (25) reverts to $X^2 + Y^2 = 27M^2$ for the Schwarzschild black hole.

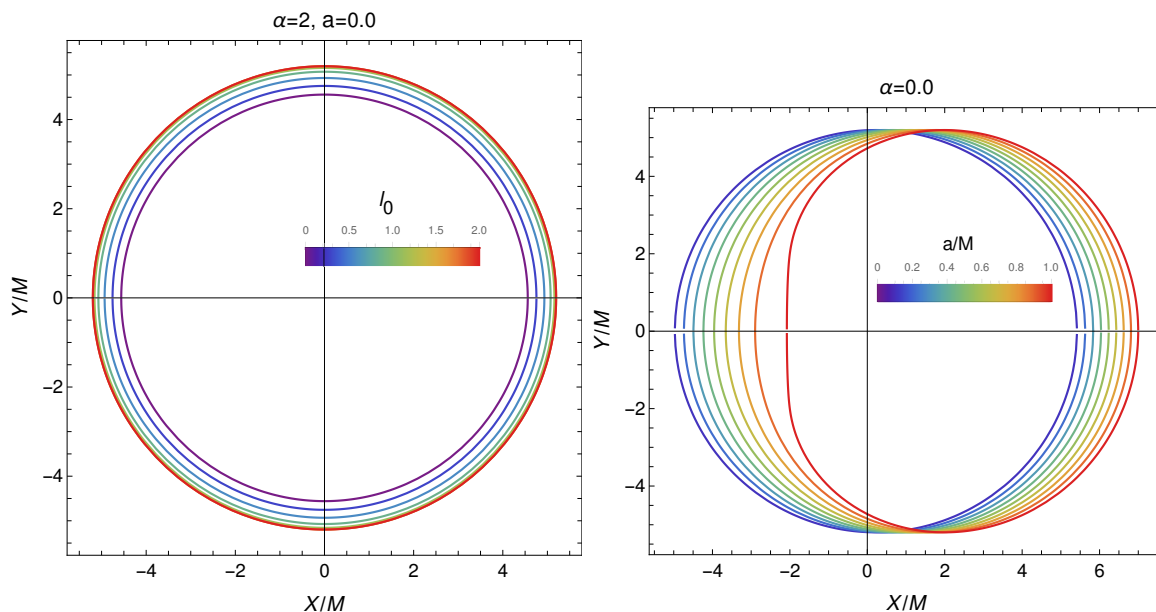


Figure 4: Shadow geometry of non-rotating hairy black holes with varying l_0 parameter (left) and Kerr black hole ($\alpha = 0$) with varying spin a (right).

The shadow for the non-rotating case ($a = 0$) and Kerr black hole ($\alpha = 0$) is depicted in Fig. 4. Whereas, a comparison of the hairy Kerr black hole shadows with that of the Kerr black hole is shown in Fig. 5. The decrease in l_0 from the Kerr limit $l_0 = l_k$, causes a decrease in the shadow size from that of the Kerr black hole (shown by the outermost solid circles in Fig. 5). Alongside this, the parameter α is found to have a decremental effect on the size of the hairy Kerr black hole shadow size, as for fixed values of a and l_0 , the shadow size decreases with the increase in α .

The presence of parameters α and l_0 has a profound influence on the approximate size and shape of the shadow (cf. Fig. 6). The shadow radius R_s of hairy Kerr black holes increases monotonically with l_0 , but interestingly α has a decremental effect, and the shadow radius of hairy Kerr black holes are always smaller than that of the Kerr black hole (solid black curve in Fig. 6), which is also evident from the shadow geometry shown in Fig. 5. Contrastingly, the distortion parameter δ_s of hairy Kerr black holes decreases with l_0 but increases with α , i.e., the shadows of hairy Kerr black holes are more distorted than the Kerr black hole (solid black curve in Fig. 6), and this trend is again inferable from Fig. 5.

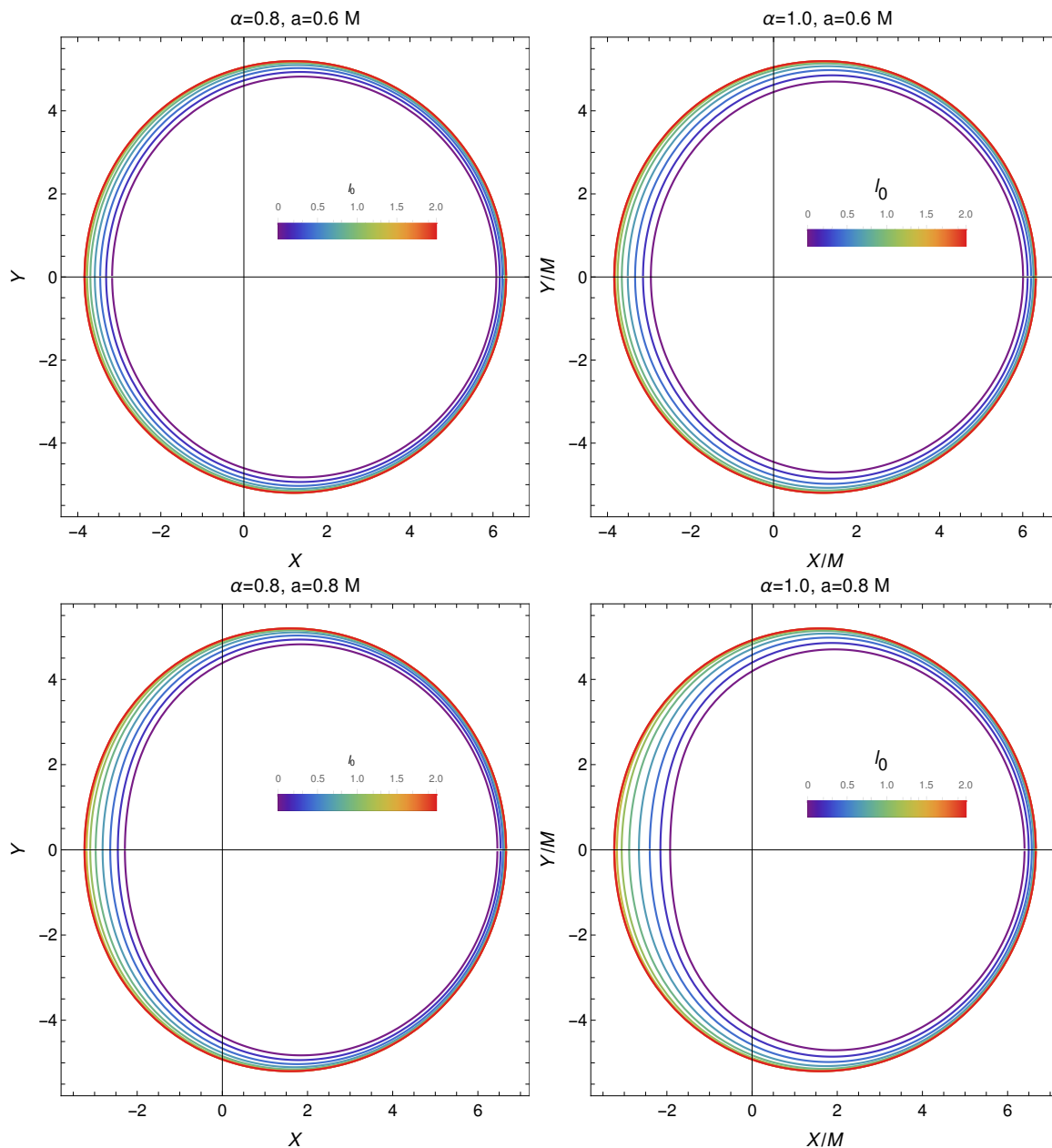


Figure 5: Shadow geometry of hairy Kerr black holes compared with Kerr black hole (outermost solid curve corresponding to $l_0 \sim l_k$).

V. OBSERVABLES AND BLACK HOLE PARAMETER ESTIMATION

The parameters associated with the hairy Kerr black holes are expected to be constrained from EHT observations. The observed image of supermassive is per the Kerr black hole of GR. However, the EHT observation did not mention black holes in modified theories [1–3]. We assume that the observer is in the equatorial plane, i.e., the inclination angle $\theta_0 = \pi/2$ for the parameter estimation.

a. Hioki and Maeda method: Hioki and Maeda [29] characterized the distortion and shadow size by proposing the two observables, viz. δ_s and R_s . They approximate the shadow by a perfect reference circle, with R_s being the radius of this circle, and δ_s , the deviation of the left edge of the shadow from the circle boundary [29]. The shadow reference circle coincides at the top (X_t, Y_t) , bottom (X_b, Y_b) and right $(X_r, 0)$ edges with the shadow contour [24].

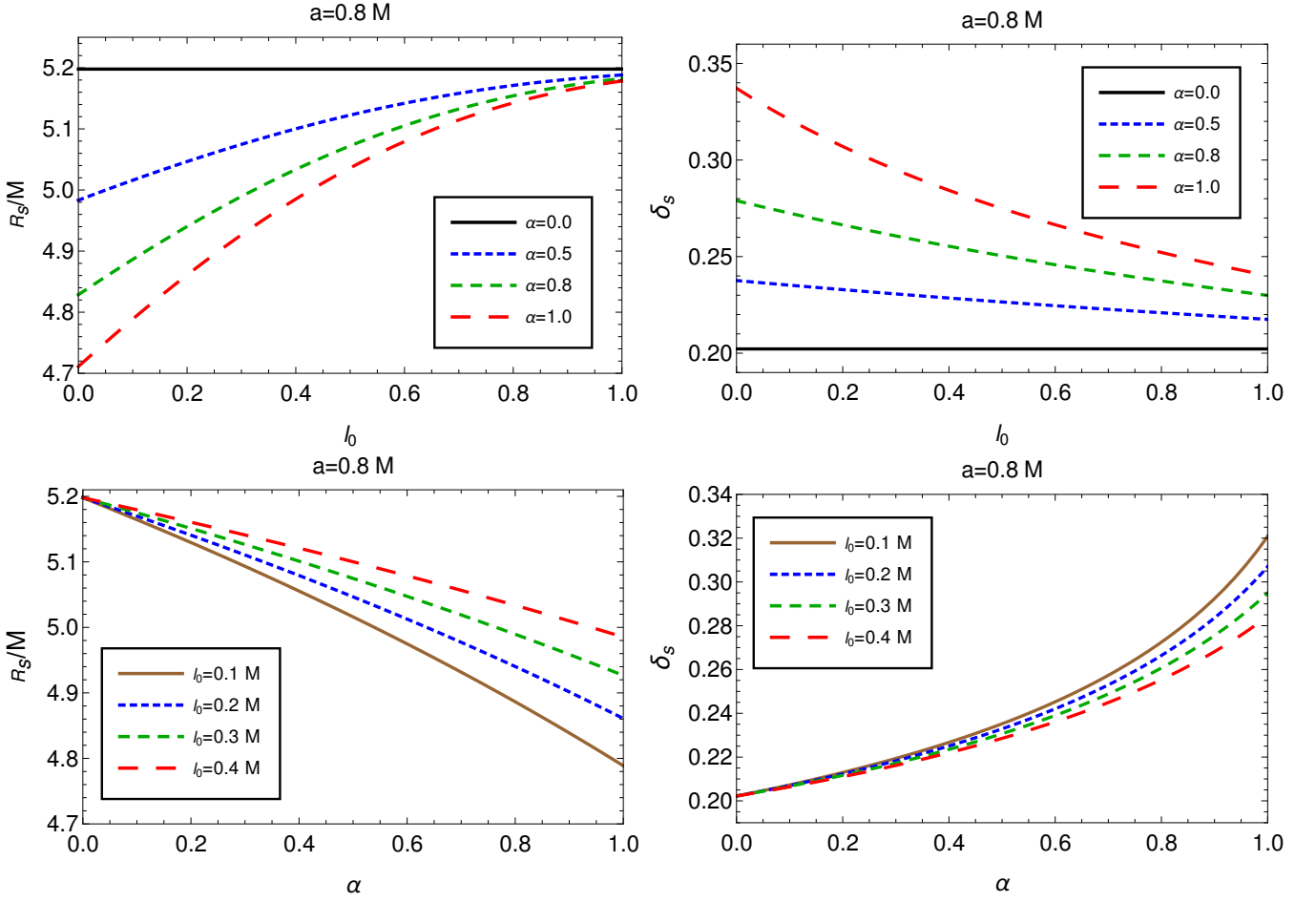


Figure 6: Variation of the shadow observables R_s (left) and δ_s (right) of the shadow of the hairy Kerr black holes.

Table I: Estimated values of hairy Kerr black hole parameters a and l_0 from known shadow observables R_s and δ_s for different values of α at inclination angle $\theta = 90^\circ$.

(a) $\alpha = 0.5$				(b) $\alpha = 1.0$			
R_s	δ_s	a/M	l_0/M	R_s	δ_s	a/M	l_0/M
5.15	0.25	0.6433	0.8255	5.10	0.004	0.6651	0.1433
5.10	0.15	0.4050	0.7147	5.045	0.035	0.5248	0.3998
5.075	0.100	0.3060	0.6214	4.90	0.15	0.2610	0.6914
5.05	0.035	0.2187	0.4028	4.80	0.40	0.1123	0.8459
5.00	0.01	0.0583	0.2220	4.75	0.70	0.0432	0.9305

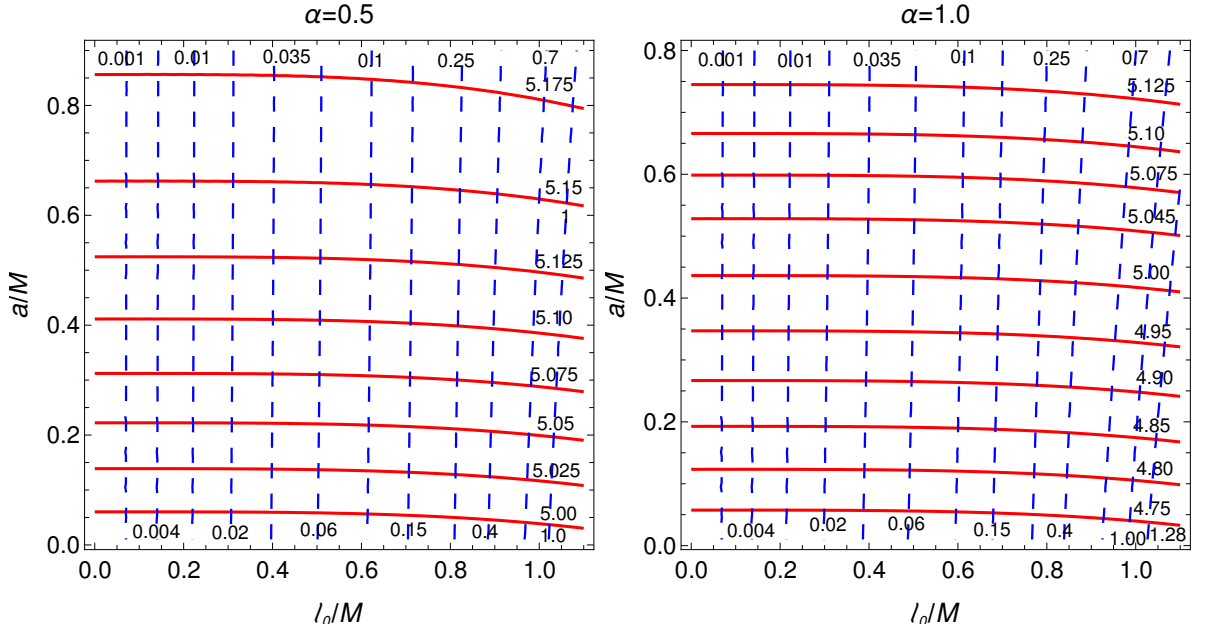


Figure 7: The contour maps for hairy Kerr black hole shadow observables R_s (red solid lines) and δ_s (blue dashed lines) at inclination angle $\theta_0 = 90^\circ$.

where, $(X'_l, 0)$ and $(X_l, 0)$ are respectively the points where the reference circle and leftmost edge of the contour of the shadow cut the horizontal axis. To estimate the black hole parameters, we plot the contours of R_s and δ_s in the $(l_0 - a)$ parameter space of the hairy Kerr black hole in Fig. 7. It is evident from the Fig. 7, the curves of radius R_s and distortion δ_s intersect each other and the intersection points for a given α depends on both a and l_0 . An intersection point of R_s and δ_s for a given α and inclination angle θ_0 , uniquely determines the parameters a and l_0 (cf. Table I). Thus, we have extended the Hioki and Maeda method [29] to uniquely determine the parameters a and l_0 of the hairy Kerr black holes.

b. Kumar and Ghosh method: The Hioki and Maeda method [29] of numerical estimation of black hole parameters using shadow observables R_s and δ_s was later extended by Tsupko [30] to analytical estimation. Further, Tsukamoto et al. [70] proposed a method to distinguish the Kerr black hole shadow from the other rotational black hole shadows arising in the MoG. However, the observables R_s and δ_s used in the above two methods demand some symmetries in the shadow shape, and they may not work precisely for the black hole shadows in modified gravity [14, 70–74]. Also, the shadow shape may not be precisely circular due to noisy data [14, 17]. Motivated by this, Kumar and Ghosh [17] presented observables characterizing a haphazard (or not circular shape) shadow to estimate the parameters associated with black holes. They defined the Area (A) and oblateness (D) by

$$A = 2 \int Y(r_p) dX(r_p) = 2 \int_{r_p^-}^{r_p^+} \left(Y(r_p) \frac{dX(r_p)}{dr_p} \right) dr_p, \quad (26)$$

and

$$D = \frac{X_r - X_l}{Y_t - Y_b}, \quad (27)$$

Indeed, while R_s designates approximately the actual size of the shadow, δ_s connotes the shadow deformation from the circular reference circle. These observables are defined as [29]

$$R_s = \frac{(X_t - X_r)^2 + Y_t^2}{2|X_r - X_t|}, \quad (28)$$

using the relations $X_b = X_t$ and $Y_b = -Y_t$, and

$$\delta_s = \frac{|X_l - X'_l|}{R_s}, \quad (29)$$

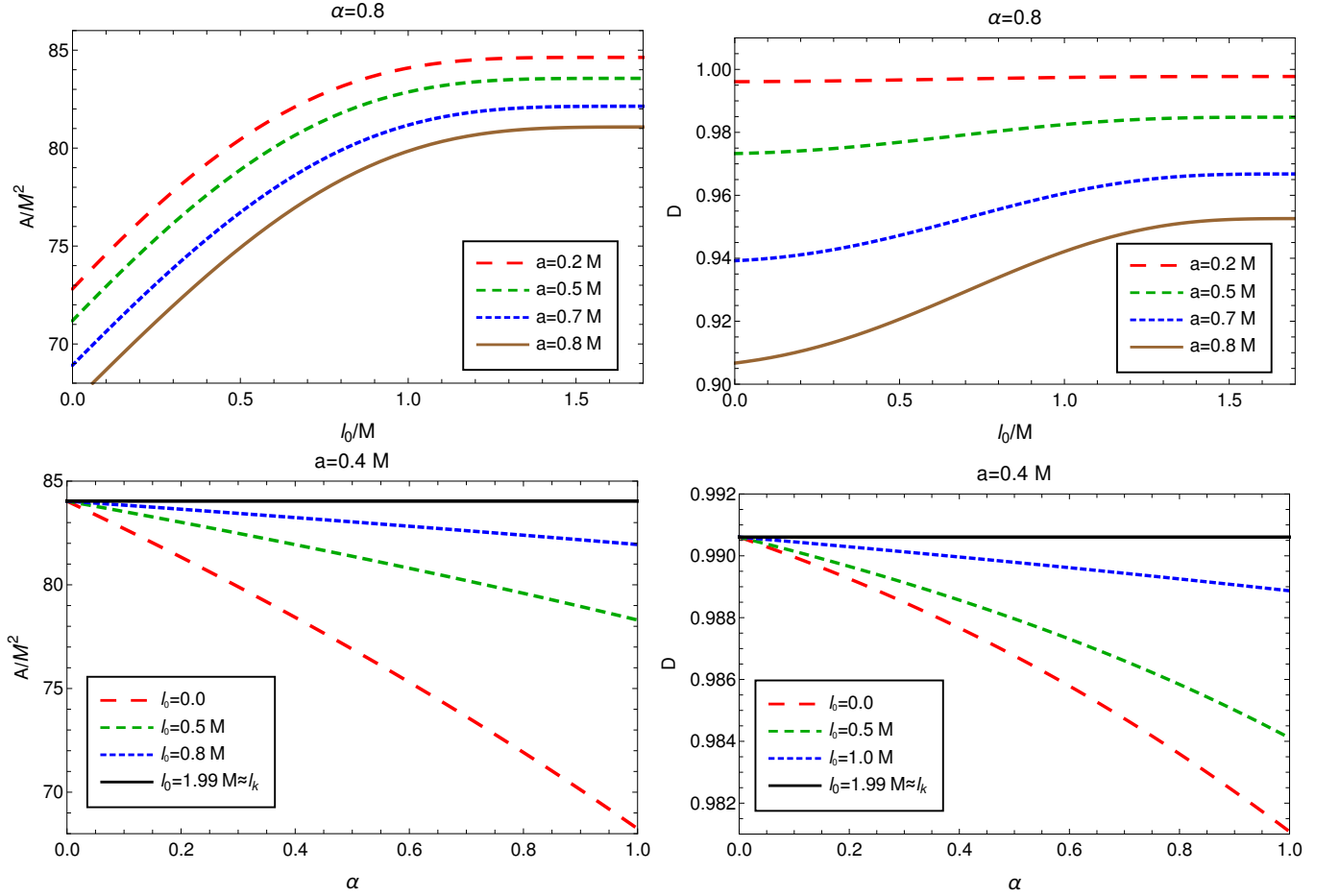


Figure 8: The shadow area A and oblateness observables D with varying parameters for the hairy Kerr black holes. The black solid line in lower panels correspond to Kerr black hole.

where subscripts r , l , t and b , respectively, stand for the right, left, top and bottom of the shadow boundary. For an equatorial observer, the distortion D may vary between $\sqrt{3}/2 \leq D < 1$, with $D = 1$ for the Schwarzschild case ($a = 0$) and $D = \sqrt{3}/2$ for extremal Kerr case ($a = M$) [74]. We plot the observables A and D in Fig. 8, and it is evident that all the three parameters a , α and l_0 have a profound impact on the shadow area. Both the area A and oblateness D increases with l_0 for fixed values of α and a and decreases with α for fixed values of l_0 and a . Both A and D decrease with a for fixed values of α and l_0 . Moreover, evidently from the lower panels in Fig. 8, the area of the hairy Kerr Black holes is smaller than that of the Kerr black hole and also is more distorted, which can also be checked from Fig. 4.

We plot the contour map of the observables A and D in the (a, l_0) plane (Fig. 9). It is clear from the Fig. 9 that the intersection point gives an exact value of parameters a and l_0 for the chosen value of A and D . In the Table II we have shown the estimated values of parameters a and l_0 of hairy Kerr black holes for given shadow observables A and D .

A. Energy Emission

Observing the shadow can lead to witnessing exciting phenomena, and in the present study, we turn to analyse the energy emission rate for hairy Kerr black holes. For an observer at infinity, the black hole shadow corresponds to a high energy absorption cross-section, which oscillates around a constant limiting value σ_{lim} for a spherically symmetric black hole. For a black hole with a photon sphere, the σ_{lim} is the same as the geometrical cross-section of the photon sphere [75] taking the form

$$\sigma_{lim} \approx \pi R_s^2. \quad (30)$$

Table II: Estimated values of hairy Kerr black hole parameters a and l_0 from known shadow observables A and D for different values of α at inclination angle $\theta_0 = 90^\circ$.

(a) $\alpha = 0.5$				(b) $\alpha = 1.0$			
A/M^2	D	a/M	l_0/M	A/M^2	D	a/M	l_0/M
84	0.998	0.1758	0.8722	84	0.998	0.1648	1.003
83	0.994	0.2961	0.7031	82	0.994	0.2657	0.7439
82	0.987	0.4211	0.6185	80	0.987	0.3666	0.6127
81	0.980	0.5061	0.5456	76	0.980	0.4203	0.3794
80	0.960	0.7089	0.8780	68	0.920	0.7230	0.1695

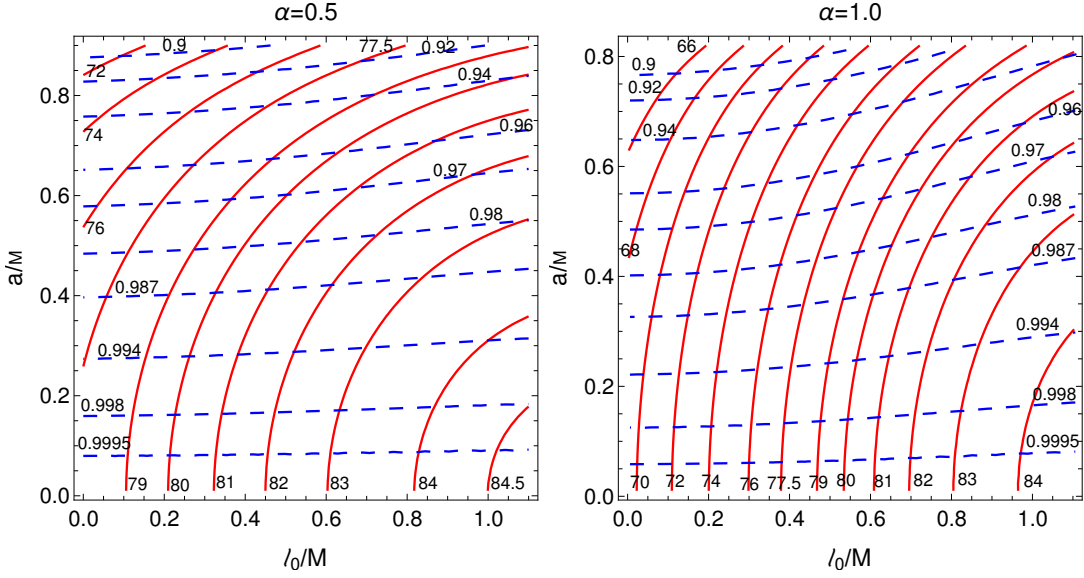


Figure 9: Contour plots of the observables A/M^2 and D in the Hairy Kerr black hole parameter space (a, l_0) with varying α . Solid red curves correspond to the constant A , and dashed blue curves are for the constant oblateness parameter D .

We intend to discuss the energy emission rate of hairy Kerr black holes which can be computed for the hairy Kerr black holes (2) using the relation [75]

$$\frac{d^2 E(\omega)}{d\omega dt} = \frac{2\pi^2 R_s^2}{e^{\omega/T} - 1} \omega^3, \quad (31)$$

where ω is photon frequency and T is the Hawking temperature at event horizon r_+ of black hole (2) given by

$$T = \frac{1}{2\pi (a^2 + r_+^2)} \left(\frac{\alpha e^{\frac{2r_+}{l_0 - 2M}} r_+ (l_0 - 2M + r_+)}{l_0 - 2M} + r_+ - M \right). \quad (32)$$

Interestingly, the Hawking temperature of hairy Kerr black holes depends on the parameter α as well as on l_0 . In Fig. 10, we plot the behaviour of the energy emission rate of hairy Kerr black holes against the photon frequency ω for various values of parameter l_0 for a given α and a . The emission rate peak decreases with an increase in l_0 and shifts to a lower value of ω while an increase.

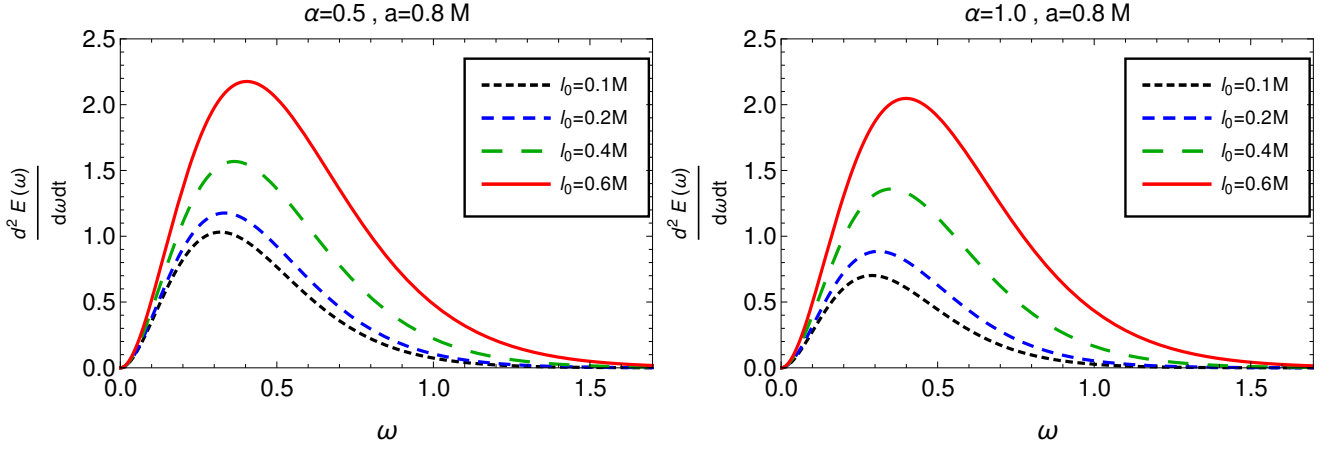


Figure 10: Evolution of the emission rate with the frequency ω for different values of parameter l_0 and a for the hairy Kerr black holes.

VI. CONSTRAINTS FROM EHT OBSERVATION OF M87*

The EHT collaboration using the VLBI technology unveiled the event horizon scale image of the supermassive black hole M87* [1–3]. This provides an exciting arena to investigate gravity in the strong-field regime to determine in turn the exact nature of black holes. The observed image of M87* is a nearly circular crescent shape; the circularity deviation is $\Delta C \leq 0.10$ (10%) and the angular size θ_d of the emission region in the observed image is $42 \pm 3 \mu\text{as}$ [1–3]. The observed image is constrained with the modelled image of Kerr black hole [1–3]. It can be further used to constrain the models of black holes in MoG.

The boundary of a black hole shadow can be defined by the polar coordinates $(R(\varphi), \varphi)$, with origin at the shadow centre (X_c, Y_c) such that $X_c = (X_r - X_l)/2$ and $Y_c = 0$. The average shadow radius \bar{R} [25] is given by

$$\bar{R} = \frac{1}{2\pi} \int_0^{2\pi} R(\varphi) d\varphi, \quad (33)$$

where

$$\bar{R} = \frac{1}{2\pi} \int_0^{2\pi} R(\varphi) d\varphi \text{ and } \varphi \equiv \tan^{-1} \left(\frac{Y}{X - X_c} \right).$$

The circularity deviation ΔC is defined as

$$\Delta C = 2 \sqrt{\frac{1}{2\pi} \int_0^{2\pi} (R(\varphi) - \bar{R})^2 d\varphi}, \quad (34)$$

The ΔC measures deviation from a perfect circle. The angular diameter of the shadow θ_d [25] is defined as

$$\theta_d = 2 \frac{R_a}{d}, \quad R_a = \sqrt{A/\pi}, \quad (35)$$

Assuming M87* a hairy Kerr black hole, we can calculate ΔC for metric (2) and use EHT observation results to put constraints on the hairy Kerr black hole parameters. We shall use the deviation from circularity defined above in Eq. (34) to perform a comparison between predicted hairy Kerr black hole shadow and the EHT observations. Assuming Kerr black hole geometry of the M87*, the EHT observations demonstrated that $\Delta C \leq 0.01$. Here we shall use hairy Kerr black hole instead. The Eq. (34) implies that the ΔC depends on the black hole metric parameters. Using mass of M87*, $M = 6.5 \times 10^9 M_\odot$ and the distance from the earth, $d = 16.8 Mpc$, the circularity deviation ΔC is depicted in Fig. 11, with the black curve denoting the EHT constraint $\Delta C = 0.10$. Clearly, the Fig. 11 indicates that the hairy Kerr black hole shadow of M87* satisfies $\Delta C \leq 0.10$ for some parameter space $(a/M, l_0/M)$.

Next we calculate diameter of the shadow, which apart from a, l_0, α, θ , depends on mass M and the distance d of the black hole. The mass of the black hole is $M \sim 6.5 \times 10^9 M_\odot$ using GR Kerr model. The angular diameter $\theta_d = 2R_s/d$, with $d = 16.8 Mpc$ for M87* for the hairy Kerr black hole is calculated and depicted in Fig. 12 as function of a and l_0 for a given $\alpha (=0.5, 1.0)$ taking inclination angle $\theta_0 = 90^\circ$.

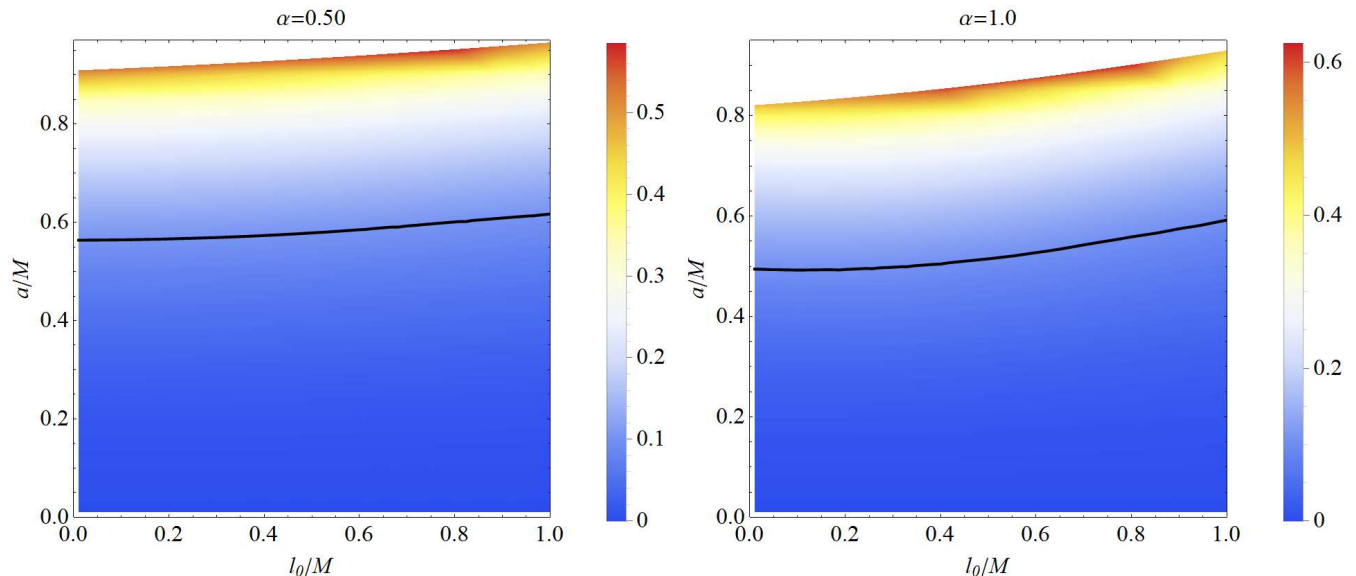


Figure 11: Circularity deviation observable ΔC for hairy Kerr black hole shadows as a function of parameters (a/M and l_0/M). The black solid curve correspond to $\Delta C = 0.01$ such that the region above the black line is excluded by the measured circularity of the M87* black hole reported by the EHT, $\Delta C \leq 0.01$. The parameters of M87* used are $M = 6.5 \times 10^9 M_\odot$, $\theta_0 = 90^\circ$ and $d = 16.8 Mpc$. The white region is forbidden for (a/M and l_0/M).

VII. CONCLUSIONS

The no-hair theorem establishes the remarkable property of general-relativistic black holes that precisely three parameters, viz. mass, spin, and charge, uniquely determine their spacetimes and, hence, all of their properties [76–79]. The spacetimes of such black holes are described by the Kerr–Newman metric [80], which reduces to the Kerr metric [81] in electrically neutral black holes or for an astrophysical black holes. Consequently, GR predicts that the Kerr metric describes all astrophysical black holes. Nonetheless, such black holes may not exist in a perfect vacuum because the presence of surrounding matter like dark matter, accretion disks could alter the Kerr nature of the black hole. Non-Kerr spacetimes incorporate potential deviations from the Kerr metric via introducing additional deviation parameters and encompasses the Kerr metric if deviation vanishes. Also, there are theoretical motivations (e.g. non-renormalizability and curvature singularities) to search for modified theories to GR. Further, The EHT collaboration captured the image of supermassive black hole M87* at 1.3 mm wavelength with an angular resolution of 20 μas thereby opening a new window to test gravity in the strong-field regime. The angular diameter of the shadow of M87* is $\theta_d = 42 \pm 3 \mu as$ exhibiting a deviation from circularity $\Delta C \leq 10$ percent and the axis ratio $\lesssim 4/3$ consistent with the Kerr black hole’s image as predicted by the GR, but the observation did not say anything about most modified gravity theories or alternatives to the Kerr black hole.

Motivated by this, we considered hairy Kerr black holes, which have additional deviation parameters α and l_0 than the Kerr black hole, and the parameter α produces deviation from Kerr geometry but with a richer configuration. It is found that the hair parameter l_0 , quantitatively has an influence on the structure of the event horizon by reducing its radius significantly with decreasing l_0 for a given α and the resulting decrease in ergosphere area is thereby likely to have impact on energy extraction, which has been investigated separately. The possibility of using the available information of M87* shadow to constraint hairy Kerr black holes, taking into account the surrounding dark matter, persuaded us to reconsider the shadow cast by the black holes. We have discussed the photons geodesics equations of motion, which are analytically solved in the first-order differential form. Observables, namely area radius R_s and oblateness δ_s , characterize the shadow size and shape and estimate the black hole parameters (a, l_0). In addition, shadow observables, namely, area A and oblateness D , are also used to explicitly determine the black hole parameters (a, l_0). Interestingly, the rotating hairy Kerr black holes, with the parameter l_0 , cast smaller and more distorted shadows, than the Kerr black holes. Interestingly, both the shadow size decreases whereas the distortion increases with the decreasing value of parameter l_0 .

The EHT observational results are used to place constraints on the hair parameter l_0 by taking the M87* black hole as the hairy Kerr black holes and using the inferred shadow angular diameter and the circularity deviation observables,

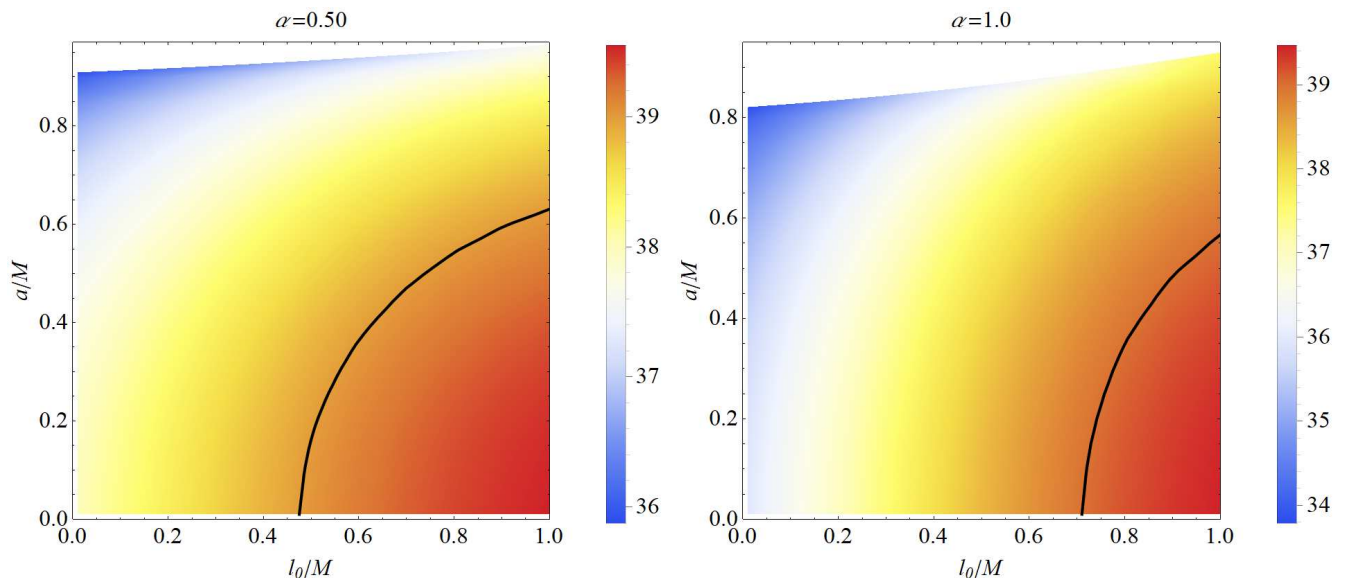


Figure 12: Angular diameter observable θ_d for hairy Kerr black hole shadows as a function of parameters (a/M and l_0/M). The black solid curve correspond to $\theta_d = 39 \mu\text{as}$ within 1σ region of the measured angular diameter of the M87* black hole reported by the EHT, $\theta_d = 42 \pm 3 \mu\text{as}$. The parameters of M87* used are $M = 6.5 \times 10^9 M_\odot$, $\theta_0 = 90^\circ$ and $d = 16.8 Mpc$. The white region is forbidden for (a/M and l_0/M).

we found that within a finite parameter space our results are in agreement with the M87* shadow. Furthermore, our results put stringent constraints on hairy Kerr black holes parameters to satisfy the M87* black hole shadow observables deduced by the EHT. Thus, the M87* shadow observations do not entirely rule out hairy Kerr black holes. The departure produced by the hairy Kerr black holes parameters l_0 and α for the M87* black hole shadow angular diameter is $\mathcal{O}(\mu\text{as})$. Hence, it is difficult to distinguish the hairy black holes from the Kerr black hole, at least from the present resolution of astronomical observations like that of the EHT, and we may have to wait for the next-generation EHT (ngEHT).

The results presented here are the generalization of previous discussions, on the Kerr black hole, to a more general setting, and demonstrate hairy Kerr black hole properties are qualitatively different from the Kerr black hole. The hairy Kerr black holes may allow studying the effect of surrounding dark matter on the Kerr black holes. One can expect that ngEHT with highly improved techniques would achieve the resolution required to observe the dark matter influence on the shadow of the black hole M87*. The black hole shadow of M87* due to EHT can also serve as a tool for distinguishing various models of theories of gravity and thereby eventually shed light on the nature of supermassive M87* and dark matter.

Acknowledgments

S.G.G. would like to thank SERB-DST for the ASEAN project IMRC/AISTDF/CRD/2018/000042. M. A. is supported by DST-INSPIRE Fellowship, Department of Science and Technology, Govt. of India

-
- [1] K. Akiyama et al., *Astrophys. J. Lett.* **875**, L1 (2019).
 - [2] K. Akiyama et al., *Astrophys. J. Lett.* **875**, L4 (2019).
 - [3] K. Akiyama et al., *Astrophys. J. Lett.* **875**, L6 (2019).
 - [4] T. Johannsen and D. Psaltis, *Astrophys. J.* **718**, (2010).
 - [5] J. L. Synge, *Mon. Not. R. astr. Soc.* **131**, (1966).
 - [6] J. P. Luminet, *Astron. Astrophys.* **75**, (1979).
 - [7] J.M. Bardeen, (1973).

- [8] H. Falcke, F. Melia and E. Agol, *Astrophys. J.* **528**, L13 (2000).
- [9] A.D. Vries, *Class. Quant. Grav.* **17**, 123 (2000).
- [10] Z. Q. Shen, K. Y. Lo, M. C. Liang, P. T. P. Ho and J. H. Zhao, *Nature* **438**, 62 (2005).
- [11] A. Yumoto, D. Nitta, T. Chiba and N. Sugiyama, *Phys. Rev. D* **86**, 103001 (2012).
- [12] F. Atamurotov, A. Abdujabbarov and B. Ahmedov, *Phys. Rev. D* **88**, 064004 (2013).
- [13] U. Papnoi, F. Atamurotov, S. G. Ghosh and B. Ahmedov, *Phys. Rev. D* **90**, 024073 (2014).
- [14] A. A. Abdujabbarov, L. Rezzolla and B. J. Ahmedov, *Mon. Not. Roy. Astron. Soc.* **454**, 2423 (2015).
- [15] F. Atamurotov, S. G. Ghosh and B. Ahmedov, *Eur. Phys. J. C* **76**, 273 (2016).
- [16] P. V. P. Cunha and C. A. R. Herdeiro, *Gen. Rel. Grav.* **50**, 42 (2018).
- [17] R. Kumar and S. G. Ghosh, *Astrophys. J.* **892**, 78 (2020).
- [18] L. Amarilla, E. F. Eiroa and G. Giribet, *Phys. Rev. D* **81**, 124045 (2010).
- [19] L. Amarilla and E. F. Eiroa, *Phys. Rev. D* **85**, 064019 (2012).
- [20] L. Amarilla and E. F. Eiroa, *Phys. Rev. D* **87**, 044057 (2013).
- [21] M. Amir, B. P. Singh and S. G. Ghosh, *Eur. Phys. J. C* **78**, 399 (2018).
- [22] B. P. Singh and S. G. Ghosh, *Annals Phys.* **395**, 127 (2018).
- [23] Y. Mizuno, Z. Younsi, C. M. Fromm, O. Porth, M. De Laurentis, H. Olivares, H. Falcke, M. Kramer and L. Rezzolla, *Nature Astron.* **2**, 585 (2018).
- [24] S. G. Ghosh, M. Amir and S. D. Maharaj, *Nucl. Phys. B* **957**, 115088 (2020).
- [25] R. Kumar and S. G. Ghosh, *JCAP* **07**, (2020).
- [26] M. Amir, B.P. Singh and S. G. Ghosh, *Eur. Phys. J. C* **78**, (2018).
- [27] E.F. Eiroa and C.M. Sendra, *Eur. Phys. J. C* **78**, 91 (2018).
- [28] I. Banerjee, S. Chakraborty and S. Sengupta, *Phys. Rev. D* **101**, 041301 (2020).
- [29] K. Hioki and K.-i. Maeda, *Phys. Rev. D* **80**, 024042 (2009).
- [30] O. Y. Tsupko, *Phys. Rev. D* **95**, 104058 (2017).
- [31] P. V. P. Cunha, C. A. R. Herdeiro, and E. Radu, *Phys. Rev. Lett.* **123**, 011101 (2019).
- [32] P. V. P. Cunha, C. A. R. Herdeiro, and E. Radu. *Universe* **5(12)**, 220 (2019).
- [33] M. Kramer, D. Backer, J. Cordes, T. Lazio, B. Stappers, and S. Johnston. *New Astron. Rev.* **48**, (2004).
- [34] E. Contreras, J. Ovalle and R. Casadio, *Phys. Rev. D* **103**, 044020 (2021).
- [35] C. A. R. Herdeiro and E. Radu, *Int. J. Mod. Phys. D* **24**, 1542014 (2015).
- [36] C. A. R. Herdeiro and E. Radu, *Phys. Rev. Lett.* **112**, 221101 (2014).
- [37] Y. X. Gao and Y. Xie *Phys. Rev. D* **103**, 043008 (2021).
- [38] C. Herdeiro, E. Radu and H. Rúnarsson, *Class. Quant. Grav.* **33**, 154001 (2016).
- [39] J. Ovalle, *Phys. Rev. D* **95**, 104019 (2017).
- [40] J. Ovalle, *Phys. Lett. B* **788**, 213 (2019).
- [41] R. Penrose and R. M. Floyd, *Nat. Phys. Sci.* **229**, (1971).
- [42] D. Pugliese and H. Quevedo, *Eur. Phys. J. C* **78**, 69 (2018)
- [43] V. P. Frolov and A. Zelnikov, *Phys. Rev. D* **90**, 124010 (2014).
- [44] B. Carter, *Phys. Rev.* **174**, (1968).
- [45] S. Chandrasekhar, *The Mathematical Theory of Black Holes* (Oxford Classic Texts in the Physical Sciences), (1983).
- [46] V. P. Frolov and A. Zelnikov, *Introduction to Black Hole Physics* (Oxford University Press), (2011).
- [47] D. C. Wilkins. *Phys. Rev. D* **5**, (1972).
- [48] H. Goldstein. *Zeitschrift für Physik* **271**, (1974).
- [49] M. Johnston and R. Ruffini, *Phys. Rev. D* **10**, (1974).
- [50] S. V. Izmailov and E. S. Levin, *Soviet Physics Journal* **22**, (1979).
- [51] S. V. Izmailov and E. S. Levin. *Soviet Physics Journal* **23**, (1980).
- [52] M. Calvani and F. de Felice, *Gen. Relativ. Gravit.* **9**, 1978.
- [53] E. Teo, *Gen. Rel. Grav.* **35**, (2003).
- [54] J. M. Bardeen, W. H. Press, and S. A. Teukolsky, *Astrophys. J.* **178**, (1972).
- [55] J. M. Bardeen and J. A. Petterson, *Astrophys. J. Lett.* **195**, L65 (1975).
- [56] R. Kumar, S. G. Ghosh and A. Wang, *Phys. Rev. D* **101**, 104001 (2020).
- [57] K. S. Virbhadra and G. F. R. Ellis, *Phys. Rev. D* **62**, 084003 (2000).
- [58] V. Bozza et al., *Gen. Relativ. Gravit.* **33**, (2001).
- [59] V. Bozza, *Phys. Rev. D* **66**, 103001 (2002).
- [60] S. G. Ghosh, R. Kumar and S. U. Islam, *JCAP* **03**, 056 (2021).
- [61] R. Kumar, S. U. Islam and S. G. Ghosh, *Eur. Phys. J. C* **80**, 1128 (2020)
- [62] S. U. Islam, R. Kumar and S. G. Ghosh, *JCAP* **09**, 030 (2020)
- [63] S. U. Islam and S. G. Ghosh, arXiv:2102.08289 [gr-qc], (2021).
- [64] A. Grenzebach, V. Perlick, and C. Lämmerzahl. *Phys. Rev. D* **89**, 124004 (2014).
- [65] P. V. P. Cunha and C. A. R. Herdeiro. *Gen. Relativ. Gravit.* **50**, (2018).
- [66] P. V. P. Cunha, C. A. R. Herdeiro, and M. J. Rodriguez. *Phys. Rev. D* **97**, 084020 (2018).
- [67] Y. Huang, Y. P. Dong, and D. J. Liu. *Int. J. Mod. Phys. B* **27(12)**, 1850114 (2018).
- [68] D. Ayzenberg and N. Yunes, *Class. Quant. Grav.* **36**, 055007 (2018).
- [69] P. V. P. Cunha, C. A. R. Herdeiro, E. Radu and H. F. Runarsson, *Phys. Rev. Lett.* **115**, 211102 (2015).
- [70] N. Tsukamoto, Z. Li and C. Bambi, *JCAP* **1406**, (2014).

- [71] A. A. Abdujabbarov, L. Rezzolla, and B. J. Ahmedov, *Int. J. Mod. Phys. D* **18**, (2009).
- [72] T. Johannsen, *Astrophys. J.* **777**, (2013).
- [73] Z. Younsi, A. Zhidenko, L. Rezzolla, R. Konoplya and Y. Mizuno, *Phys. Rev.D* **94**, 084025 (2016).
- [74] Tsupko, O. Yu, *Phys. Rev.D* **95**, 104058 (2017).
- [75] S. W. Wei and Y. X. Liu, *JCAP* **063**, (2013).
- [76] W. Israel, *Phys. Rev.* **164**, 1776 (1967).
- [77] W. Israel, *Commun. Math. Phys.* **8**, 245 (1968).
- [78] B. Carter, *Commun. Math. Phys.* **26**, 331 (1971).
- [79] S.W. Hawking, *Commun. Math. Phys.* **25**, 152 (1972).
- [80] E.T. Newman, E. Couch, K. Chinnapared, A. Exton, A. Prakash, R. Torrence, *J. Math. Phys.* **6**, 918 (1965).
- [81] R. P. Kerr, *Phys. Rev. Lett.* **11**, (1963).